Topological thermal transport of sliding electron crystals

Ning-Jing Yang, Zhigao Huang, and Jian-Min Zhang*
Fujian Provincial Key Laboratory of Quantum Manipulation and New Energy Materials, College of Physics and Energy, Fujian Normal University, Fuzhou 350117, China

(Received 17 December 2025; revised 23 February 2026; accepted 13 March 2026; published 8 April 2026)

Topological thermal transport offers a quantum route to regulate heat flow through Berry-curvature-driven responses. However, approaches for dynamically switchable control of such transport are lacking. Here, we propose an interlayer-sliding-driven dynamical evolution mechanism to control topological thermal transport in bilayer antiferromagnetic electron crystals, exemplified by ScI_2. Sliding breaks spin group symmetry, generates ferroelectric polarization, and reshapes layer-resolved Berry curvature, resulting in strong modulation of anomalous Nernst and thermal Hall conductivities as signatures of topological phase transitions. Giant thermal Hall peaks and Hall plateaus emerge under sliding, demonstrating amplified topological heat transport response. Reversing the sliding direction switches spin splitting and transport polarity, enabling direct reading of stacking order and motion direction. Our work uncovers topological thermoelectric characteristics and superior transport performance in sliding systems, providing new insights for thermoelectric device design and applications.

DOI: 10.1103/2qs3-ssjz

I. INTRODUCTION

In electronic systems, the interplay between crystal structure and magnetic order governs the topological and transport properties of materials. For example, the quantum anomalous Hall effect in magnetic materials reflects not only the band topology but also manifests as quantized transverse transport characteristics [1–7]. Similarly, topological thermoelectric effects, analogous to the electrical Hall effect, generate transverse charge and heat currents under a temperature gradient, corresponding to the anomalous Nernst effect and the anomalous thermal Hall effect, respectively [8–13]. Topological thermoelectric transport is determined by the intrinsic Berry curvature of the system, which is generally proportional to the spontaneous magnetization, and has been extensively studied in time-reversal-symmetry-broken ferromagnets and, more recently, in altermagnets [14–17]. However, in multilayer antiferromagnets, the vanishing macroscopic magnetization suppresses anomalous thermoelectric transport, posing challenges for their thermoelectric investigations.

For multilayer magnetic materials, particularly antiferromagnets, an out-of-plane electric field can induce the layer Hall effect [18–22]. Similarly, the layer Hall effect can also be realized through sliding ferroelectricity, which, unlike an external electric field, arises intrinsically from charge-transfer-induced polarization potential in the crystal [23–29]. In bilayer antiferromagnetic systems, existing studies have primarily focused on employing sliding ferroelectricity to tune topological phase transitions [26,30]. In terms of transport, most attention has been devoted to the spin Hall and charge Hall effects [26,31–33], while investigations of thermoelectric transport driven by sliding ferroelectricity remain highly insufficient. More importantly, the intrinsic mechanical dynamics during the interlayer sliding process have been largely overlooked, with most results restricted to specific stacking configurations. Among current control strategies, approaches that involve genuine dynamical processes are still rare, making the dynamical characteristics of interlayer sliding a topic of pressing importance.

In this work, we present the dynamical evolution of topological thermoelectric transport induced by interlayer sliding in bilayer antiferromagnetic systems. From a symmetry perspective, interlayer sliding breaks the $\{C_2 \parallel m_z\}$ spin-space group symmetry, which not only induces spin splitting but also generates an interlayer sliding ferroelectric polarization potential. During the sliding dynamics, this polarization potential continuously modulates the spin-resolved bands and the layer-resolved spin Berry curvature. By evaluating the anomalous Nernst and anomalous thermal Hall conductivities, we show that bilayer antiferromagnets exhibit finite topological thermoelectric transport once the symmetry is broken. Moreover, the thermoelectric response is directly correlated with the sliding direction: reversing the sliding direction leads to opposite anomalous thermoelectric signals. We further demonstrate that the topological thermoelectric response serves as a clear indicator of sliding-induced topological phase transitions. For the anomalous thermal Hall effect, we uncover both a robust Hall-conductivity plateau and a pronounced giant thermal Hall peak. Our results highlight not only the dynamical control of topological thermoelectric transport by sliding ferroelectricity in bilayer antiferromagnets, but also the great potential of thermal Hall signals as probes of topological phases and for practical applications.

II. COMPUTATIONAL DETAILS

First-principles simulations were performed using the Vienna *Ab initio* Simulation Package (VASP) [34,35], based on the framework of density functional theory (DFT). The exchange-correlation interactions were described by the

*Contact author: jmzhang@fjnu.edu.cn

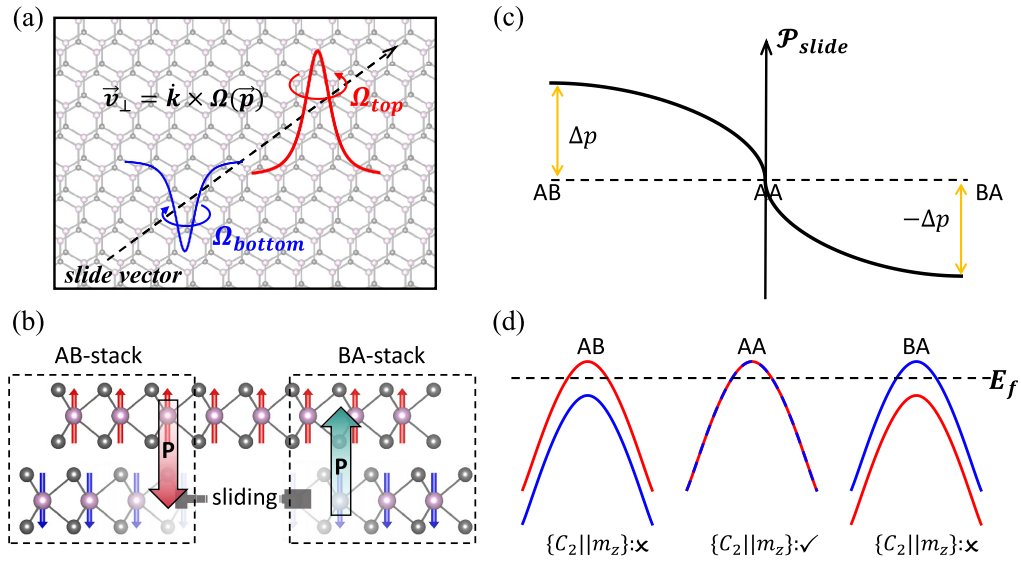

FIG. 1. (a) Schematic illustration of Berry curvature dynamics in a bilayer sliding ferroelectric lattice. (b) Diagram of sliding ferroelectricity in bilayer antiferromagnets. (c) Variation of the interlayer polarization potential with sliding. (d) Spin-split bands with spin-layer locking. Red (blue) denotes the top-layer up spin (bottom-layer down spin). The $\{C_2||m_z\}$ symmetry is preserved (✓) or broken (✗) depending on the sliding, and the dashed line marks the Fermi level E_f.

Perdew-Burke-Ernzerhof (PBE) functional within the generalized gradient approximation (GGA) scheme [36,37]. A vacuum region of 15 Å was applied along the out-of-plane direction to eliminate interlayer interactions in the two-dimensional model. The plane-wave basis was truncated at a kinetic energy cutoff of 500 eV, and the Brillouin zone was sampled using an $11 \times 11 \times 1$ Monkhorst Pack k-point mesh. The structures were fully relaxed until the total energy difference was less than 10^{-6} eV and the residual forces on each atom were below 0.01 eV/Å. The symmetry parities of the occupied bands were identified using the IRREP code [38]. In addition, maximally localized Wannier functions (MLWFs) were constructed with the WANNIER90 package, and the corresponding tight-binding Hamiltonian was generated and analyzed using WANNIERTOOLS [39,40]. Additional results are provided in the Supplemental Material [41] (see also Ref. [42] therein).

III. RESULTS AND DISCUSSION

In a two-dimensional bilayer system, interlayer sliding shifts the center of mass and thereby induces an interlayer ferroelectric polarization potential. Under this polarization potential, the quantum geometry associated with the layer degree of freedom is modified. Specifically, sliding ferroelectricity breaks the layer symmetry, resulting in layer-dependent modifications of the Berry curvature and a nontrivial quantum geometry. By contrast, the intralayer quantum metric remains largely unaffected. Within linear response theory, the in-plane transverse Hall conductivity is also altered by the sliding-induced ferroelectric polarization potential, as illustrated in Fig. 1(a). Due to the interlayer polarization, the Berry curvature variations in the upper and lower layers are opposite in sign, leading to an enhancement in one layer and a suppression in the other. A prototypical example of sliding ferroelectricity is realized in two-dimensional hexagonal lattices, particularly in bilayer antiferromagnets. As shown in Fig. 1(b), by fixing the upper layer and laterally sliding the lower antiferromagnetic spin layer, one can achieve the stacking transitions among AB, AA, and BA configurations. Moreover, opposite sliding directions generate interlayer ferroelectric polarization potentials of opposite orientations, as depicted in Fig. 1(c). The sliding ferroelectric polarization potential originates from the change of polarization before and after interlayer sliding calculated via first-principles Berry-phase method, reflecting the electronic charge redistribution and acting as an effective potential on the low-energy electronic states. Notably, interlayer sliding can be experimentally controlled using Kelvin probe force microscopy (KPFM) under different bias conditions [23,43–45]. This process allows access to stable sliding configurations and does not significantly affect the static transport responses after sliding.

In the nonsliding AA stacking, the system preserves the $\{C_2||m_z\}$ spin symmetry, which guarantees the degeneracy of the up and down spins. With the ferroelectric polarization potential generated by interlayer sliding, the band structure exhibits spin splitting due to the breaking of the $\{C_2||m_z\}$ symmetry. As the sliding direction is reversed, the orientation of the sliding-induced ferroelectric polarization potential also changes, leading to opposite spin splittings or polarizations in the AB and BA stackings, as shown in Fig. 1(d).

This type of sliding ferroelectric effect is generally applicable in hexagonal lattices. For bilayer antiferromagnetic MX_2 and MA_2Z_4 families, the above conclusions hold during the sliding process. As a representative example, we select ScI_2, a candidate material that exhibits a pronounced sliding ferroelectric polarization [29], to discuss the band structure and thermoelectric properties driven by sliding ferroelectricity. According to the sliding configuration shown in Fig. 1(a), we first calculate the band structures of three representative

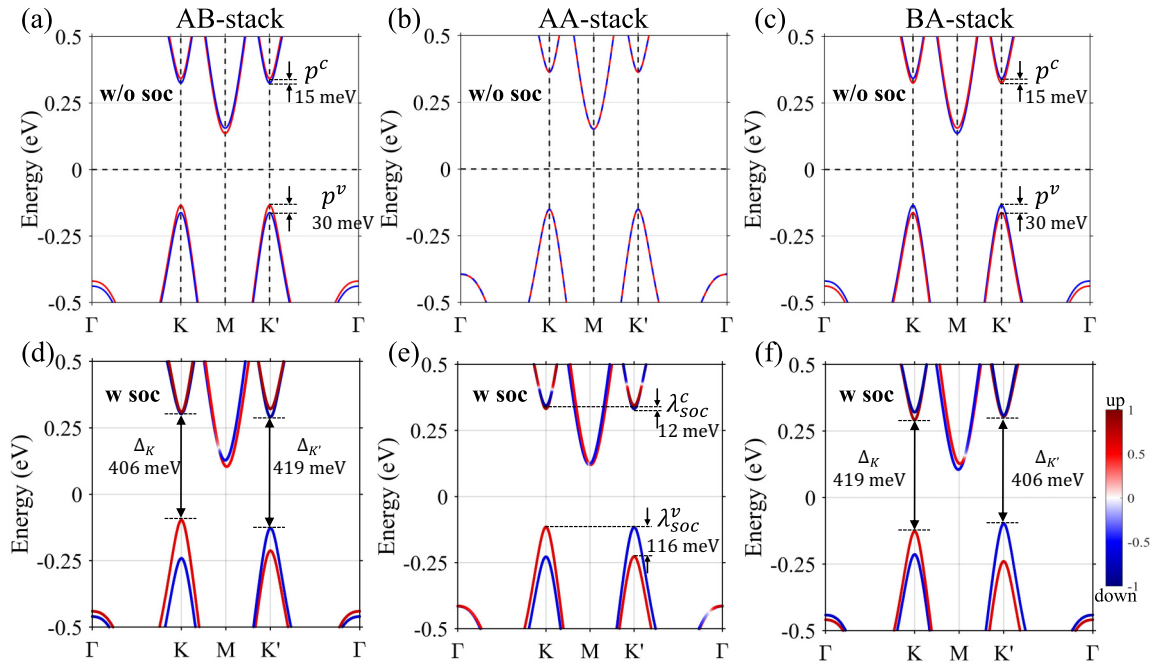

FIG. 2. Spin-resolved band structures of bilayer antiferromagnetic ScI_2 without SOC for the AB (a), AA (b), and BA (c) stackings. Panels (d)–(f) show the corresponding spin-projected band structures with SOC.

stacking arrangements during the sliding process. As shown in Fig. 2(a), the symmetry breaking induced by sliding gives rise to spin splitting. Without considering spin-orbit coupling (SOC), the spin bands in the AA stacking remain degenerate, as displayed in Fig. 2(b). When sliding to the AB and BA stackings, the spin splittings appear with opposite signs in the two cases, as shown in Figs. 2(a) and 2(c). Due to the different orbital contributions at the conduction-band minimum and the valence-band maximum, the magnitudes of the splittings p_v and p_c are not equal. When SOC is included, the AA-stacked antiferromagnetic ScI_2 still shows no spin polarization, as shown in Fig. 2(e). Meanwhile, the band structures under sliding reveal that, in the AB stacking, the gap at the K valley for spin-up electrons is smaller than that at the K' valley for spin-down electrons, indicating spin polarization, as displayed in Fig. 2(d). Figure 2(f) presents the opposite result for the BA stacking, where the gap of the spin-down channel becomes smaller.

Next, to reveal the layer-resolved Berry curvature in the sliding ferroelectric system, we construct a multi-orbital-based sliding ferroelectric Hamiltonian [29],

$$\mathcal{H} = \sum_{\langle ij\rangle}\sum_{\alpha\beta s} t_{ij}^{\alpha\beta} c_{i\alpha s}^{\dagger} c_{j\beta s} + \sum_{i\alpha s} \epsilon_{i\alpha} c_{i\alpha s}^{\dagger} c_{i\alpha s} + \sum_{i\alpha\beta s} \boldsymbol{\lambda}^{z}_{\boldsymbol{\alpha\beta s}} c_{i\alpha s}^{\dagger} c_{i\beta s} + \sum_{i\alpha s} \boldsymbol{P}_{\boldsymbol{\alpha s}} c_{i\alpha s}^{\dagger} c_{i\alpha s} + \text{H.c.}, \quad (1)$$

where $c_{i\alpha}^{\dagger}$ ($c_{j\beta}$) denotes the creation (annihilation) operator of an electron in orbital α (β) located at site i (j). The term ϵ_α specifies the on-site potential of orbital α, and $t_{ij}^{\alpha\beta}$ represents the nearest-neighbor hopping amplitude between orbitals on sites i and j. The third term incorporates the atomic intrinsic SOC, expressed as $\boldsymbol{\lambda}^{z}_{\boldsymbol{\alpha\beta s}} = \lambda_I \boldsymbol{L}^{z}_{\boldsymbol{\alpha\beta}} s^{z}_{s}$. The final term accounts for the sliding ferroelectric contribution, defined as $\boldsymbol{P}_{\boldsymbol{\alpha s}} = \boldsymbol{P}_{\boldsymbol{\alpha}} s_z$.

Owing to the locking between spin and layer degrees of freedom, the layer-resolved Berry curvature is equivalent to the spin-resolved Berry curvature. The spin-resolved Berry curvature can then be calculated using the following expression:

$$\Omega_n^{s,z}(\boldsymbol{k}) = -2\hbar^2 \sum_{n\neq n'} \frac{\text{Im}\,\langle\psi_{nk}|\hat{v}_x|\psi_{n'k}\rangle\langle\psi_{n'k}|\hat{v}_y|\psi_{n\boldsymbol{k}}\rangle}{\left(E^s_{n'} - E^s_n + i0^+\right)^2}, \quad (2)$$

where $\hat{v}_i (i = x, y)$ is the velocity operator. s is the spin index, corresponding to the same spin channel. Consequently, the Berry curvature with spin-layer locking, obtained from the above calculation, is shown in Fig. 3. For the upper layer carrying spin-up states, the sliding ferroelectric polarization potential enhances the Berry curvature at the K and K' valleys, as shown in Fig. 3(a). In contrast, the sliding ferroelectric potential exerts an opposite effect on the lower layer relative to the upper one, leading to a decrease in its Berry curvature with sliding, as shown in Fig. 3(b). Because pristine ScI_2 possesses a large band gap, the changes in Berry curvature induced by sliding are not very pronounced; however, as illustrated by the magnified view of the valleys, the variation trend is clearly visible. A more significant effect can be realized when the band gap is reduced under applied strain. To further reveal this effect, we consider applying a longitudinal temperature gradient along the x axis of the bilayer AFM ScI_2 film, as illustrated in Fig. 4(a). This generates a transverse current in the y direction:

$$J_y^e = \alpha_{xy} \nabla_x T. \quad (3)$$

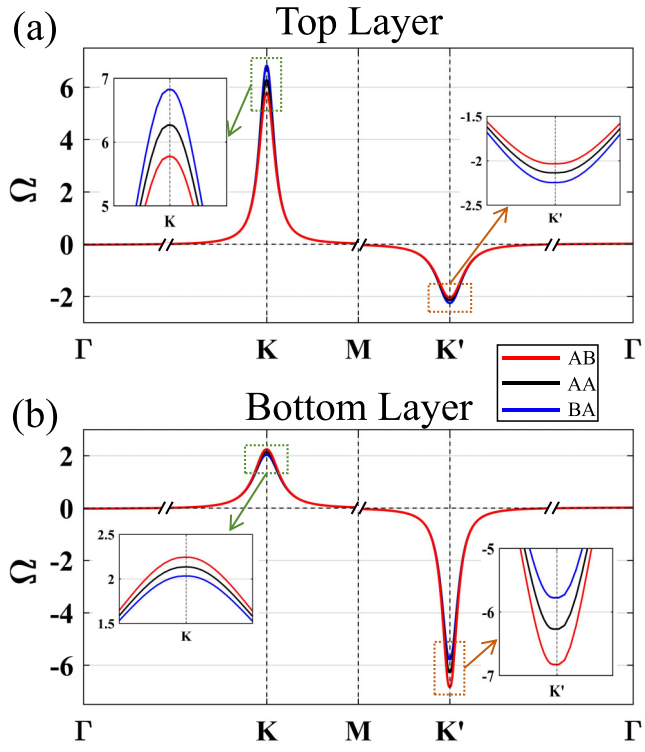

FIG. 3. Berry curvatures of the top layer (a) and bottom layer (b) in bilayer antiferromagnetic ScI_2 under different stackings during the sliding process.

The anomalous Nernst conductivity α_{xy} is given by [46,47]

$$\alpha_{xy} = \frac{ek_B}{\hbar}\sum_n \int \frac{d^2k}{(2\pi)^2}\Omega^n S(\mathbf{k}), \tag{4}$$

where the entropy density is defined as $S(\mathbf{k}) = -f\ln f - (1-f)\ln(1-f)$. Here, f denotes the Fermi-Dirac distribution function. It is worth noting that $S(\mathbf{k})$ exhibits a peak at the Fermi level E_F, while it essentially vanishes when the energy lies outside the range $[E_F - 5k_BT,\ E_F + 5k_BT]$. Therefore, α_{xy} is mainly determined by the band structure within an energy window of about $10k_BT$ around the Fermi level.

In addition to driving the transverse anomalous Nernst conductivity, the applied temperature gradient also induces a transverse heat current under the anomalous thermal Hall effect:

$$J_y^Q = -\kappa_{xy}\nabla_x T. \tag{5}$$

The anomalous thermal Hall conductivity κ_{xy} is defined as [48–50]

$$\kappa_{xy} = \frac{k_B^2 T}{\hbar}\sum_n \int \frac{d^2k}{(2\pi)^2}\Omega^n F(\mathbf{k}), \tag{6}$$

where the weighting function $F(\mathbf{k}) = \frac{\pi^2}{3} + (\frac{E-E_F}{k_BT})^2 f - 2\,\mathrm{Li}_2(1-f) - [\ln(1+e^{-(E-E_F)/(k_BT)})]^2$. Here, $\mathrm{Li}_n(x) = \sum_{m=1}^{\infty}\frac{x^m}{m^n}$ denotes the polylogarithm function, and we take $n = 2$. This expression corresponds to the intrinsic thermal Hall conductivity with the energy magnetization correction properly taken into account, following the formalism of Qin *et al.* [49].

The $2H$ vdW structure results in pronounced spin-associated ferroelectric polarization, especially at the K/K' valley positions. To elucidate and simplify the thermoelectric regulation of the bilayer antiferromagnetic system driven by sliding ferroelectricity, a low-energy effective model is employed to capture the essential physics. Consequently, the effective Hamiltonian for the spin- and layer-locked sliding ferroelectric system near the Dirac cone is expressed as

$$\begin{aligned}\hat{H} = {} & at(\tau k_x\hat{\sigma}_x + k_y\hat{\sigma}_y) + \frac{\Delta_E}{2}\hat{\sigma}_z \\ & - \lambda\tau\frac{\hat{\sigma}_z - \chi_\lambda}{2}\hat{s}_z + p\frac{\hat{\sigma}_z - \chi_p}{2}\hat{s}_z.\end{aligned} \tag{7}$$

Here, $\tau = \pm 1$ denotes the valley index, 2λ represents the spin splitting at the top of the valence band due to spin-orbit coupling (SOC), and p signifies the interlayer ferroelectric polarization induced by bilayer sliding. χ_λ and χ_p describe the asymmetry between the valence and conduction bands due to spin-orbit coupling and sliding ferroelectricity, respectively. σ represents the Pauli matrices for the energy bands in the two basis functions. a is the lattice constant, t is the hopping integral, Δ_E is the band gap, and $\mathbf{s}$ represents the spin Pauli matrices. These terms describe the asymmetry between the conduction and valence bands due to SOC and ferroelectric polarization, with their values ranging from 0 to 1. The energy eigenvalues $E_{n\tau s_z} = n\sqrt{(kat)^2 + (\frac{\Delta_E - s_z\lambda\tau + s_z p}{2})^2} + s_z\frac{p\chi_p}{2} + s_z\frac{\lambda\tau\chi_\lambda}{2}$, where $s_z = \pm 1$ denotes the spin index and $n = \pm 1$ indicates the band index. Then, we can obtain the Berry curvature associated with the valley

$$\Omega_\tau^n(\mathbf{k}) = -\tau n\frac{2a^2t^2\Delta_m}{[4(kat)^2 + (\Delta_m)^2]^{(3/2)}}, \tag{8}$$

where $\Delta_m = \Delta_E - s_z\lambda\tau - s_z p$. In this manner, the valley-resolved α_{xy} and κ_{xy} can be obtained.

We begin by analyzing the thermoelectric response of a single layer, corresponding to one spin channel. Because the Berry curvature at the K and K' valleys has opposite signs, the anomalous Nernst conductivity in a monolayer also changes sign with the variation of the Fermi level. As the temperature increases, the entropy density becomes larger, which in turn enhances α_{xy}, as shown in Fig. 4(b). Unlike the weighting function of the S function, the different weighting of the F function causes the thermal flow to start accumulating from about $5k_BT$ below E_F, thereby inducing a thermal Hall plateau inside the band gap. With further temperature increase, owing to the characteristics of the F function, the plateau width decreases accordingly, as shown in Fig. 4(c). In Figs. 4(b) and 4(c), varying temperature does not alter the essential transport features; therefore, finite-temperature effects do not affect the determination of phase transitions based on thermal transport responses.

When the bilayer antiferromagnet undergoes interlayer sliding, the ferroelectric polarization potential associated with the sliding induces spin splitting, which in turn generates a difference in the Berry curvatures between the top and bottom layers. As a result, both the transverse electric and thermal transport respond accordingly: the transport signals in the top

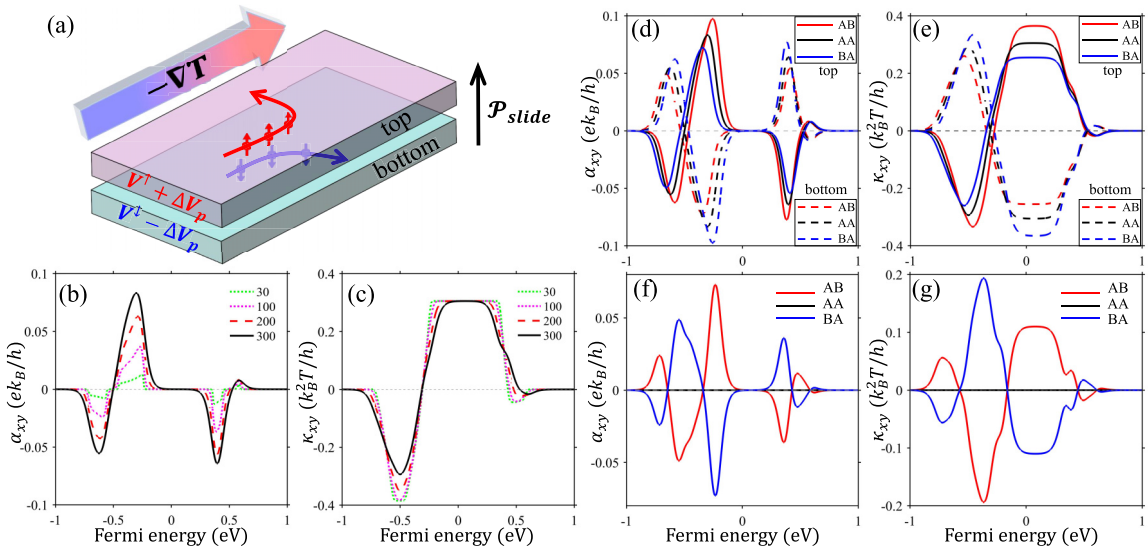

FIG. 4. (a) Schematic of a thermal Hall effect device based on a sliding bilayer antiferromagnet. (b) The anomalous Nernst conductivity of the upper layer as a function of Fermi energy at different temperatures. (c) The anomalous thermal Hall conductivity of the upper layer as a function of Fermi energy at different temperatures. Layer-resolved anomalous Nernst conductivity (d) and anomalous thermal Hall conductivity (e) for different stacking configurations under sliding. Red, black, and blue curves correspond to AB, AA, and BA stackings, respectively. Solid and dashed lines denote the upper and lower layers. Total anomalous Nernst conductivity (f) and anomalous thermal Hall conductivity (g) of the antiferromagnetic bilayer as functions of Fermi energy for different stacking configurations.

layer increase with the ferroelectric potential, while those in the bottom layer behave oppositely, as shown in Figs. 4(d) and 4(e). Notably, in the AA stacking, spin degeneracy is protected by symmetry, which leads to equal-magnitude but opposite-sign Hall signals in the two layers. Consequently, the overall α_{xy} and κ_{xy} of the bilayer system vanish. When the ferroelectric polarization potential breaks the $\{C_2 \parallel m_z\}$ symmetry, spin splitting induces distinct electric and thermal responses in the two layers, resulting in nonzero α_{xy} and κ_{xy}. Moreover, opposite sliding directions produce opposite ferroelectric polarizations and spin splittings, causing the anomalous Nernst conductivities of AB and BA stackings to have opposite signs, as shown in Fig. 4(f). The same behavior also applies to the anomalous thermal Hall conductivity, as shown in Fig. 4(g). Due to the valley degree of freedom, different spin channels contribute oppositely to the transport response, and their relative magnitudes can be tuned by interlayer sliding. As a result, the AB and BA stacking configurations exhibit mirror-symmetric transport signals. As shown in Figs. 4(f) and 4(g), the sign reversal of the thermoelectric response is determined by the sliding direction. Therefore, transverse thermoelectric transport offers a probe of the stacking order and sliding direction in bilayer antiferromagnets. On the other hand, sliding-induced spin splitting can also affect the longitudinal thermal transport to some extent. However, in contrast to the transverse thermal Hall response, the longitudinal thermal conductivity is primarily governed by the band dispersion and Fermi velocities, and can be expressed as $\kappa_{xx} = \frac{e^2\tau}{hT}\sum_{n,k} v_{n,x}^2(E_{n,k}-\mu)^2(-\frac{\partial f}{\partial E})$. Since the overall distribution of Fermi velocities changes only marginally upon sliding, the resulting modification of the longitudinal thermal conductivity is much weaker than the sliding-induced modulation of the transverse thermal conductivity.

In addition to distinguishing sliding directions and stacking configurations, anomalous thermoelectric signals can also serve as probes of topological phases in ScI_2 and related materials. For bilayer antiferromagnetic ScI_2, which hosts a variety of topological phases, extensive studies have been carried out in previous work [29]. In particular, its spin-resolved and asynchronous topological evolution under ferroelectric sliding has been highlighted. Figure 5(a) schematically illustrates this process: the sliding ferroelectricity tunes the band gap, leading to successive higher-order topological phase transitions for spin-up and spin-down channels. Owing to the strong layer-resolved character of this system, a novel spin-hybrid topological phase emerges, in which one spin channel realizes a first-order phase while the other remains in a second-order phase. The corresponding boundary states are shown in Fig. 5(b), where only a single edge state connects the valence and conduction bands. The spatial configuration of the spin-hybrid topological insulator (SHTI) is presented in Fig. 5(c), with one layer exhibiting a second-order phase and the other a first-order phase. The Wilson loop along the k_x direction, plotted in Fig. 5(d), further confirms this distinction: the spin-up channel carries a Chern number of 1, while the spin-down channel retains the fractional polarization characteristic of a SOTI.

By tuning the band gap, five distinct phases—SOTI, SHTI, QSHI, QAHI, and NI—can be realized. The detection and distinction of these phases have long been central issues. During a topological phase transition, a band inversion occurs at a valley, leading to distinct Berry curvatures associated with each topological phase. Consequently, these phases exhibit different thermoelectric transport responses, which are reflected in the anomalous Nernst conductivity and anomalous thermal Hall conductivity. In bilayer antiferromagnetic ScI_2,

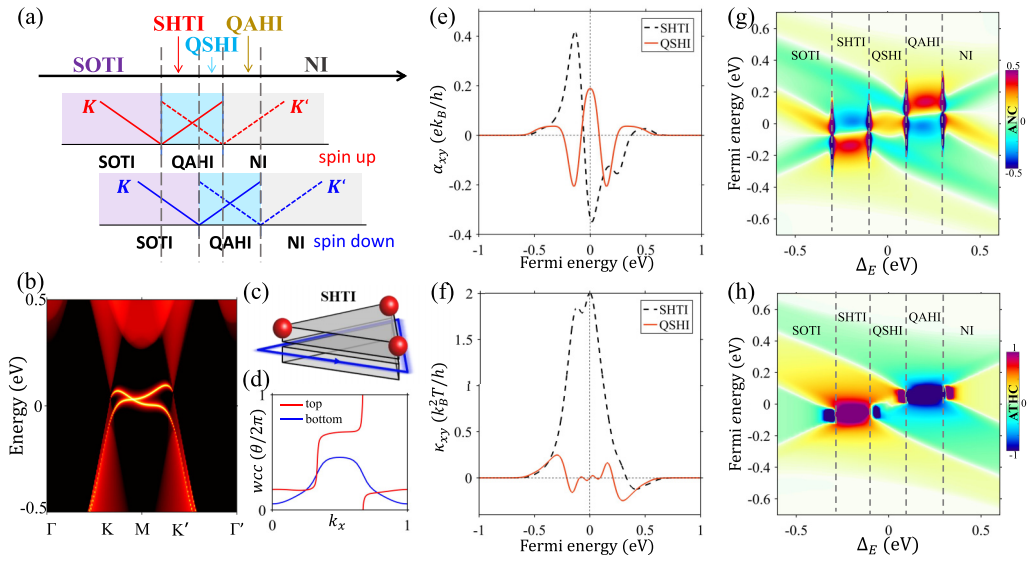

FIG. 5. (a) Schematic illustration of the sliding ferroelectricity-induced asynchronous topological phase transition. (b) Surface states of the SHTI. (c) Real-space schematic of the SHTI. (d) Spin-resolved Wannier charge center (WCC) of the SHTI. Comparison of the anomalous Nernst conductivity (e) and anomalous thermal Hall conductivity (f) between the SHTI and QSHI, represented by black dashed and orange solid lines, respectively. Topological phase diagrams of a bilayer AFM sliding ferroelectric system characterized by the anomalous Nernst (g) and anomalous thermal Hall (h) effects, both plotted as functions of band gap modulation.

the SHTI and QSHI phases show characteristic differences in their α_{xy} and κ_{xy} near the Fermi level, as displayed in Figs. 5(c) and 5(d). To provide a more systematic comparison of the thermoelectric transport in different topological phases, we continuously tune the parameter ΔE and calculate the corresponding phase diagram characterized by α_{xy} and κ_{xy}. As shown in Figs. 5(g) and 5(h), clear phase boundaries are identified, and each topological phase is further distinguished by its unique thermoelectric signals. The horizontal axis Δ_E in the figure represents strain-induced tuning under a fixed sliding ferroelectric polarization. Thus, sliding-induced thermal transport in bilayers also serves as an effective probe for identifying different phases. Beyond ScI_2, the predicted topological thermoelectric effects remain applicable to other materials that satisfy the required symmetry conditions, such as the MX_2 and MA_2X_4 families [26,33,51]. Moreover, a larger sliding ferroelectric potential leads to more pronounced physical signatures. Experimentally, the band gap and topological phases of two-dimensional materials can be tuned via controllable strain, such as using flexible substrates or micro-/nano-mechanical loading techniques, which have been demonstrated in a variety of two-dimensional systems [52–54]. Meanwhile, interlayer sliding ferroelectricity has been directly observed in bilayer van der Waals materials, and the sliding states can be distinguished and manipulated using scanning probe techniques or electrical measurements [43–45]. Therefore, the proposed topological thermal Hall response is experimentally accessible and can serve as an effective physical signature for identifying sliding ferroelectric states.

By tuning the sliding vector, distinct spin splittings are induced in the band structure, which constitute the physical origin of the sliding-dependent thermal transport signals. In contrast, band dispersion modulation alone generally affects only the magnitude of the thermal conductivity. Numerically, sliding mainly redistributes the electronic Berry curvature near the valley regions, thereby strongly modulating the transverse thermal conductivity, while the longitudinal component remains weakly affected. Experimentally, in antiferromagnetic systems such as Mn_3Sn, the transverse thermal Hall response has likewise been shown to be dominated by electronic Berry curvature [55,56]. Accordingly, the sliding-induced Berry curvature redistribution can be considered the primary mechanism responsible for the variation of κ_{xy}. From the thermal Hall phase diagram in Fig. 5, one can see that reaches or even exceeds the upper limit of the color scale near the phase boundaries. Notably, in the SHTI and QAHI phases, a wide energy window maintains values close to the maximum. By extracting a representative segment of, we identify a pronounced Hall peak that is significantly higher than in other phases, highlighting the strong thermoelectric response of the sliding bilayer system, as shown in Fig. 6. For a typical two-dimensional thin-film thickness, the predicted anomalous thermal Hall conductivity corresponds to the order of 10^2 W Km, representing a relatively high magnitude among experimentally reported anomalous thermal Hall responses [11,57]. Such a giant Hall conductivity not only amplifies the transverse thermoelectric conversion efficiency but also provides a promising platform for designing high-sensitivity Hall sensors and low-power topological electronic devices. This giant Hall response reflects an enhanced Berry curvature concentration near the band edges, implying a strong tunability of topological transport under sliding ferroelectric control. In addition, the sliding lattice also exhibits a stable thermal transport feature—a Hall plateau—reflecting the stability of thermoelectric signals in specific phases. This extended Hall plateau signifies the persistence of transverse thermal transport over a wide energy range, demonstrating remarkable steadiness against perturbations. The presence of sliding ferroelectricity further enables the plateau to be shifted and

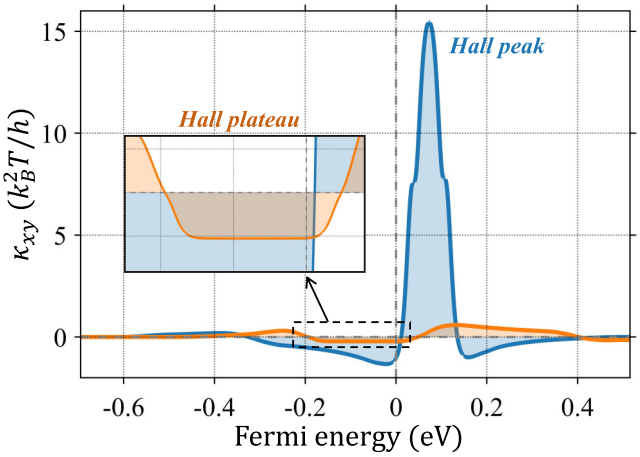

FIG. 6. Giant anomalous thermal Hall peak and Hall plateau in the bilayer antiferromagnetic system.

tuned, offering an effective means to control thermal flow and optimize thermoelectric performance in layered topological systems. This plateau behavior, together with the pronounced Hall peak, reveals that the sliding system not only reshapes the band topology but also stabilizes the associated thermoelectric transport.

IV. CONCLUSIONS

In summary, we have investigated the dynamical evolution of topological thermal transport driven by interlayer sliding in bilayer antiferromagnetic electron crystals. The sliding process breaks the spin group symmetry and induces a ferroelectric polarization potential, which continuously tunes the spin-resolved band structure and layer-resolved Berry curvature. As a consequence, distinct transverse thermoelectric responses emerge, including anomalous Nernst and thermal Hall conductivities that serve as fingerprints of topological phase transitions. The thermal Hall response exhibits giant peaks and plateaus, reflecting the redistribution of Berry curvature across the bilayer. Moreover, the reversal of sliding direction leads to opposite spin splitting and thermoelectric signals, providing a direct probe of stacking order and sliding direction. These findings demonstrate that sliding ferroelectricity enables dynamical control of Berry curvature and topological thermal transport in layered antiferromagnets. More broadly, the demonstrated mechanism highlights that interlayer sliding can serve as a general dynamic knob for engineering topological and thermoelectric functionalities in two-dimensional magnets, offering new opportunities for realizing motion-driven quantum devices where heat, spin, and topology are coherently intertwined.

ACKNOWLEDGMENTS

This work is mainly supported by the National Natural Science Foundation of China (Grants No. 11874113, No. 62474041, and No. 12274078) and the Natural Science Foundation of Fujian Province of China (Grants No. 2025J02018 and No. 2023J01519).

DATA AVAILABILITY

The data that support the findings of this article are not publicly available. The data are available from the authors upon reasonable request.

[1] Y. Deng, Y. Yu, M. Z. Shi, Z. Guo, Z. Xu, J. Wang, X. H. Chen, and Y. Zhang, Quantum anomalous Hall effect in intrinsic magnetic topological insulator $MnBi_2Te_4$, Science **367**, 895 (2020).

[2] Y. Tokura, K. Yasuda, and A. Tsukazaki, Magnetic topological insulators, Nat. Rev. Phys. **1**, 126 (2019).

[3] C.-L. Chiu, T. Wang, R. Fan, K. Watanabe, T. Taniguchi, X. Liu, M. P. Zaletel, and A. Yazdani, High spatial resolution charge sensing of quantum Hall states, Proc. Natl. Acad. Sci. USA **122**, e2424781122 (2025).

[4] H. Sun, B. Xia, Z. Chen, Y. Zhang, P. Liu, Q. Yao, H. Tang, Y. Zhao, H. Xu, and Q. Liu, Rational design principles of the quantum anomalous Hall effect in superlatticelike magnetic topological insulators, Phys. Rev. Lett. **123**, 096401 (2019).

[5] C.-Z. Chang, C.-X. Liu, and A. H. MacDonald, *Colloquium*: Quantum anomalous Hall effect, Rev. Mod. Phys. **95**, 011002 (2023).

[6] W. Huynh, B. Liu, S. Munyan, S. Ahadi, and S. Stemmer, Chiral edge state control of thermoelectric effects, Sci. Adv. **11**, eady9006 (2025).

[7] G. Xu, B. Lian, and S.-C. Zhang, Intrinsic quantum anomalous Hall effect in the kagome lattice $Cs_2LiMn_3F_{12}$, Phys. Rev. Lett. **115**, 186802 (2015).

[8] C. Fu, Y. Sun, and C. Felser, Topological thermoelectrics, APL Mater. **8**, 040913 (2020).

[9] Y. Pan, C. Le, B. He, S. J. Watzman, M. Yao, J. Gooth, J. P. Heremans, Y. Sun, and C. Felser, Giant anomalous Nernst signal in the antiferromagnet $YbMnBi_2$, Nat. Mater. **21**, 203 (2022).

[10] D. Gong, J. Yang, S. Zhang, S. Pandey, D. Cui, J. P. Ruff, L. Horak, E. Karapetrova, J.-W. Kim, P. J. Ryan, *et al.*, Large asymmetric anomalous Nernst effect in the antiferromagnet $SrIr_{0.8}Sn_{0.2}O_3$, Nat. Commun. **16**, 2888 (2025).

[11] H. Zhang, C. Xu, C. Carnahan, M. Sretenovic, N. Suri, D. Xiao, and X. Ke, Anomalous thermal Hall effect in an insulating van der Waals magnet, Phys. Rev. Lett. **127**, 247202 (2021).

[12] Y. Gu, Y. Gu, F. Liu, S. Ohira-Kawamura, N. Murai, and J. Zhao, Signatures of Kitaev interactions in the van der Waals ferromagnet VI_3, Phys. Rev. Lett. **132**, 246702 (2024).

[13] T. Yokoi, S. Ma, Y. Kasahara, S. Kasahara, T. Shibauchi, N. Kurita, H. Tanaka, J. Nasu, Y. Motome, C. Hickey, *et al.*, Half-integer quantized anomalous thermal Hall effect in the Kitaev material candidate α-$RuCl_3$, Science **373**, 568 (2021).

[14] L. Zhang, Berry curvature and various thermal Hall effects, New J. Phys. **18**, 103039 (2016).

[15] R. R. Neumann, A. Mook, J. Henk, and I. Mertig, Thermal Hall effect of magnons in collinear antiferromagnetic

insulators: Signatures of magnetic and topological phase transitions, Phys. Rev. Lett. **128**, 117201 (2022).
[16] L. Xu, X. Li, X. Lu, C. Collignon, H. Fu, J. Koo, B. Fauqué, B. Yan, Z. Zhu, and K. Behnia, Finite-temperature violation of the anomalous transverse Wiedemann-Franz law, Sci. Adv. **6**, eaaz3522 (2020).
[17] X. Zhou, W. Feng, R.-W. Zhang, L. Šmejkal, J. Sinova, Y. Mokrousov, and Y. Yao, Crystal thermal transport in altermagnetic RuO_2, Phys. Rev. Lett. **132**, 056701 (2024).
[18] A. Gao, Y.-F. Liu, C. Hu, J.-X. Qiu, C. Tzschaschel, B. Ghosh, S.-C. Ho, D. Bérubé, R. Chen, H. Sun, *et al.*, Layer Hall effect in a 2D topological axion antiferromagnet, Nature (London) **595**, 521 (2021).
[19] L. L. Tao, Q. Zhang, H. Li, H. J. Zhao, X. Wang, B. Song, E. Y. Tsymbal, and L. Bellaiche, Layer Hall detection of the Néel vector in centrosymmetric magnetoelectric antiferromagnets, Phys. Rev. Lett. **133**, 096803 (2024).
[20] W. Du, K. Dou, X. Li, Y. Dai, Z. Wang, B. Huang, and Y. Ma, Topological layer Hall effect in two-dimensional type-I multiferroic heterostructure, Nat. Commun. **16**, 6141 (2025).
[21] R. Chen, H.-P. Sun, M. Gu, C.-B. Hua, Q. Liu, H.-Z. Lu, and X. Xie, Layer Hall effect induced by hidden Berry curvature in antiferromagnetic insulators, Nat. Sci. Rev. **11**, nwac140 (2024).
[22] Y. Han, Y. Guo, Z. Li, and Z. Qiao, Layer Hall effect without external electric field, Phys. Rev. Lett. **134**, 236206 (2025).
[23] M. Wu and J. Li, Sliding ferroelectricity in 2D van der Waals materials: Related physics and future opportunities, Proc. Natl. Acad. Sci. USA **118**, e2115703118 (2021).
[24] X. Han and X. Zhao, Stackingtronics: Programmable interlayer sliding in 2D materials, Nano Lett. **25**, 16955 (2025).
[25] Y. Feng, Y. Dai, B. Huang, L. Kou, and Y. Ma, Layer Hall effect in multiferroic two-dimensional materials, Nano Lett. **23**, 5367 (2023).
[26] Y. Tian, C.-B. Wang, B.-Y. Zhang, X. Kong, and W.-J. Gong, Quantum layer spin Hall effect in sliding antiferromagnetic bilayers, J. Mater. Chem. C **12**, 10950 (2024).
[27] H. Cheng, H. Chen, G. Hu, X. Yuan, J. Ren, and X. Zhao, Electrical control of the valley-layer Hall effect in ferromagnetic bilayer lattices, J. Phys. Chem. Lett. **15**, 8759 (2024).
[28] A. Anirban, Quantum anomalous layer Hall effect, Nat. Rev. Phys. **5**, 271 (2023).
[29] N.-J. Yang, J.-M. Zhang, X.-P. Li, Z. Zhang, Z.-M. Yu, Z. Huang, and Y. Yao, Sliding ferroelectrics induced hybrid-order topological phase transitions, Phys. Rev. Lett. **134**, 256602 (2025).
[30] Y. Liang, P. Zhao, F. Zheng, and T. Frauenheim, Sliding ferroelectric controllable topological phases in the $Bi_2Te_3/MnBi_2Te_4$ heterobilayer, Phys. Rev. B **111**, 035444 (2025).
[31] J. Ma, X. Luo, and Y. Zheng, Strain engineering the spin-valley coupling of the R-stacking sliding ferroelectric bilayer $2H$-VX_2(X = S, Se, Te), npj Comput. Mater. **10**, 102 (2024).
[32] T. Zhang, X. Xu, B. Huang, Y. Dai, L. Kou, and Y. Ma, Layer-polarized anomalous Hall effects in valleytronic van der Waals bilayers, Mater. Horiz. **10**, 483 (2023).
[33] Z. Gao, L. Chen, J. Chen, Z. Luo, X. Li, Z. Niu, J. Shi, T. Cao, and X. Fan, Ferroelectric control of layer-polarized anomalous Hall effects in bilayer and trilayer $RuCl_2$, Mater. Today Phys. **46** 101473 (2024).
[34] G. Kresse and J. Furthmüller, Efficient iterative schemes for *ab initio* total-energy calculations using a plane-wave basis set, Phys. Rev. B **54**, 11169 (1996).
[35] G. Kresse and J. Furthmüller, Efficiency of *ab-initio* total energy calculations for metals and semiconductors using a plane-wave basis set, Comput. Mater. Sci. **6**, 15 (1996).
[36] J. P. Perdew, K. Burke, and M. Ernzerhof, Perdew, Burke, and Ernzerhof reply, Phys. Rev. Lett. **80**, 891 (1998).
[37] J. P. Perdew, K. Burke, and M. Ernzerhof, Generalized gradient approximation made simple, Phys. Rev. Lett. **77**, 3865 (1996).
[38] M. Iraola, J. L. Mañes, B. Bradlyn, M. K. Horton, T. Neupert, M. G. Vergniory, and S. S. Tsirkin, IrRep: Symmetry eigenvalues and irreducible representations of *ab initio* band structures, Comput. Phys. Commun. **272**, 108226 (2022).
[39] A. A. Mostofi, J. R. Yates, Y.-S. Lee, I. Souza, D. Vanderbilt, and N. Marzari, Wannier90: A tool for obtaining maximally-localised Wannier functions, Comput. Phys. Commun. **178**, 685 (2008).
[40] Q. Wu, S. Zhang, H.-F. Song, M. Troyer, and A. A. Soluyanov, Wanniertools: An open-source software package for novel topological materials, Comput. Phys. Commun. **224**, 405 (2018).
[41] See Supplemental Material at http://link.aps.org/supplemental/10.1103/2qs3-ssjz for (I) projected band structure, (II) sliding ferroelectric polarization potential, (III) tight-binding model, (IV) topological phase transition, (V) comparison with the hybrid functional, (VI) Wannier fitting with DFT, (VII) sliding energy, which includes Ref. [42].
[42] X. Liu, A. P. Pyatakov, and W. Ren, Magnetoelectric coupling in multiferroic bilayer VS_2, Phys. Rev. Lett. **125**, 247601 (2020).
[43] P. Meng, Y. Wu, R. Bian, E. Pan, B. Dong, X. Zhao, J. Chen, L. Wu, Y. Sun, Q. Fu, *et al.*, Sliding induced multiple polarization states in two-dimensional ferroelectrics, Nat. Commun. **13**, 7696 (2022).
[44] F. Sui, H. Li, R. Qi, M. Jin, Z. Lv, M. Wu, X. Liu, Y. Zheng, B. Liu, R. Ge, *et al.*, Atomic-level polarization reversal in sliding ferroelectric semiconductors, Nat. Commun. **15**, 3799 (2024).
[45] M. Vizner Stern, Y. Waschitz, W. Cao, I. Nevo, K. Watanabe, T. Taniguchi, E. Sela, M. Urbakh, O. Hod, and M. Ben Shalom, Interfacial ferroelectricity by van der Waals sliding, Science **372**, 1462 (2021).
[46] D. L. Bergman and V. Oganesyan, Theory of dissipationless Nernst effects, Phys. Rev. Lett. **104**, 066601 (2010).
[47] X.-Q. Yu, Z.-G. Zhu, G. Su, and A.-P. Jauho, Thermally driven pure spin and valley currents via the anomalous Nernst effect in monolayer group-VI dichalcogenides, Phys. Rev. Lett. **115**, 246601 (2015).
[48] T. Yokoyama and S. Murakami, Transverse magnetic heat transport on the surface of a topological insulator, Phys. Rev. B **83**, 161407(R) (2011).
[49] T. Qin, Q. Niu, and J. Shi, Energy magnetization and the thermal Hall effect, Phys. Rev. Lett. **107**, 236601 (2011).
[50] B. Zhou, R. Zeng, B. Zhou, X. Zhou, K. Yang, and G. Zhou, Light-induced anomalous Hall, Nernst, and thermal Hall effects in black phosphorus thin films, Phys. Rev. B **110**, 125411 (2024).
[51] Y.-Q. Li, X. Zhang, X. Shang, Q.-W. He, D.-S. Tang, X.-C. Wang, and C.-G. Duan, Magnetic and ferroelectric manipulation of valley physics in Janus piezoelectric materials, Nano Lett. **23**, 10013 (2023).

[52] Z. Dai, L. Liu, and Z. Zhang, Strain engineering of 2D materials: Issues and opportunities at the interface, Adv. Mater. **31**, 1805417 (2019).

[53] H. J. Conley, B. Wang, J. I. Ziegler, R. F. Haglund, Jr., S. T. Pantelides, and K. I. Bolotin, Band gap engineering of strained monolayer and bilayer MoS_2, Nano Lett. **13**, 3626 (2013).

[54] Z. Li, Y. Lv, L. Ren, J. Li, L. Kong, Y. Zeng, Q. Tao, R. Wu, H. Ma, B. Zhao, *et al.*, Efficient strain modulation of 2D materials via polymer encapsulation, Nat. Commun. **11**, 1151 (2020).

[55] X. Li, L. Xu, L. Ding, J. Wang, M. Shen, X. Lu, Z. Zhu, and K. Behnia, Anomalous Nernst and Righi-Leduc effects in Mn_3Sn: Berry curvature and entropy flow, Phys. Rev. Lett. **119**, 056601 (2017).

[56] H. Chi, Y. Ou, T. B. Eldred, W. Gao, S. Kwon, J. Murray, M. Dreyer, R. E. Butera, A. C. Foucher, H. Ambaye, *et al.*, Strain-tunable Berry curvature in quasi-two-dimensional chromium telluride, Nat. Commun. **14**, 3222 (2023).

[57] T. Ideue, T. Kurumaji, S. Ishiwata, and Y. Tokura, Giant thermal Hall effect in multiferroics, Nat. Mater. **16**, 797 (2017).